Chapter 3

OBSERVATIONS AND ANALYSIS

3.1 The Ooty Radio Telescope

The observations described in this thesis were made using the Ooty Radio Telescope (ORT) at the Radio Astronomy Centre, Ooty. This telescope operates at a frequency of 326.5 MHz with a bandwidth of 4 MHz. The ORT, which has been described in detail by Swarup *et al.* (1971), is used for various astronomical studies. Currently, a major fraction of its daytime use is dedicated to interplanetary-scintillation studies of compact radio sources. IPS observations of weakly-scintillating radio sources require a telescope of large collecting area which is capable of tracking a source for sufficient time in order to obtain stable power spectra having high signal-to-noise ratios. The ORT, which has an effective collecting area of $\sim 8000\,m^2$ and can track a radio source continuously for about 10 hours, is well suited for IPS studies.

The ORT is a parabolic cylindrical antenna, 530 m long in the north-south direction and 30 m wide in east-west. The reflecting surface of the ORT is formed by 1100 thin stainless-steel wires. The antenna is equatorially mounted, its long north-south axis lying parallel to the axis of rotation of the Earth. This is achieved

by mounting the cylinder on a north-south hillside of inclination +11°22′50″ to the horizontal. The latitude of Ooty is also 11°22′50″N. Hence, it is possible to track a source by mechanically rotating the cylinder about its north-south axis. The telescope can cover an hour-angle range of –4h to $+5\frac{1}{2}$h.

An array of 1056 dipoles is placed along the focal line of the parabolic cylindrical reflector. Groups of 48 dipoles form 22 electronic modules that constitute the feed system of the telescope. Each dipole is connected through 4-bit radio-frequency (RF) diode phase-shifters used to set the observing declination (Joshi *et al.* 1988), to a "Christmas-Tree" feeder system. The phase-shifters are controlled by a PDP-11/24 computer, which is also responsible for data acquisition. The beam of each module can be tilted in the north-south direction by introducing appropriate phase shifts between the successive dipoles in each half module, the outputs of pairs of half modules being combined to form the beams of the single modules. The signals from all 22 modules are corrected for module-to-module delay and phase differences at the IF stage. In this way, a declination coverage of $\delta = \pm 36°$ is achieved. For observations outside this declination range, the IF delays are not adequately compensated and hence the sensitivity drops sharply.

One of the important features of the ORT is the availability of twelve beams in the North-South direction. Any two the adjacent beams are separated by $3' sec(\delta)$ in declination. Thus, the twelve beams projected on the sky cover $36' sec(\delta)$ in declination, making the ORT particularly useful for survey-type observations. For IPS observations, this multi-beam coverage is used for monitoring both the source and off-source regions simultaneously. For beam-formation, the output of each module is subdivided into twelve equal parts at IF and each output is delayed appropriately with respect to other modules by suitable lengths of cables, to give a 3′ shift in declination at the equator. This results in 12 × 22 outputs that are

combined appropriately to form the twelve beams.

Each beam of the ORT can be operated in both total-power and correlation modes. In the correlation mode, the output of the northern half of the telescope is cross-correlated (multiplied) with that of the southern half. In the total-power mode, the outputs of the northern and southern halves of the telescope are summed. The half-power beamwidth for both these modes is about 2° in the east-west direction, while in the north-south direction, the beam width is about $3.9' sec(\delta)$ for the correlation mode and about $5.5' sec(\delta)$ for the total-power mode. Although the sensitivity in the correlation mode is $\sqrt{2}$ times poorer than in the total-power mode (Kraus, 1966), the correlation mode is preferred for IPS observations since it provides more stable baselines. Further, in the correlation mode the level of interference is considerably less as most of the interference that arises locally does not correlate between the two halves of the telescope.

3.2 The IPS Observations

The IPS observations presented in this thesis were taken with a central beam (Beam 6) of the ORT in the correlation mode, using a 50-ms time constant. After detection, the output is fed to a 12-bit analog-to-digital convertor (ADC), which is interfaced to the on-line PDP-11/24 computer. The output of Beam 6 is also sent to a chart recorder and these chart records used as a visual monitor. In addition, two adjacent beams of the correlation system, Beams 5 and 7, and an off-source total-power beam (such as Beam 10) of the ORT are also displayed on the chart recorder, principally to monitor interference. The total-power off-source beam provides a full record of all interference and is very useful for eliminating contaminated records when editing the data.

The output of Beam 6 is sampled by the computer every 20 *ms* and recorded on magnetic tape. Each data record on the tape contains 2600 data points, representing 52 *s* of data. During the on-line data acquisition, the mean and r.m.s of each record are typed on a computer terminal, giving an immediate indication of the scintillation level and the system performance. Observations of each source are taken for about 20 – 30 *min*. An off-source observation with Beam 6 gives a reference zero level. This reference level would include the effects of background radiation from the sky and any of the offsets introduced by the receiver system. The difference between the mean intensity levels of on- and off-source gives a deflection proportional to the flux density of the observed source. It is essential to have a good off-source record for an accurate determination of scintillation index (see eqns. 2.2 and 2.5) Normally, an off-source observation is made once per 90 *min* by tracking a cold region of sky with the random phases set for the dipoles of the feed. The r.m.s of the scintillations can be computed by integrating the area under the observed power spectrum and taking its square root (see Section 2.4, eqn. 2.5). This r.m.s can also be computed using the on- and off-source variances by,

$$rms \;=\; (VAR_{ON} \;-\; VAR_{OFF})^{\frac{1}{2}} \tag{3.1}$$

In the present study, we use the area under the power spectrum for the determination of the scintillation index.

An extensive series of observations was made during 1986 – 89 at solar elongations greater than 4° ($\geq 16R_0$) on many strongly-scintillating radio sources. These sources cover a large range of heliographic latitude and heliocentric distances, hence enabling the study of the three-dimensional structure of the solar-wind. The angular structures of most of the sources observed are known from other high-resolution observations such as VLBI.

3.3 The Power Spectrum of the Intensity Fluctuations

The most convenient method of analysing a large amount of intensity-fluctuation data is to perform a power-spectrum analysis. For IPS data this is a useful technique for bringing out the statistical properties of the IP medium. In the following sections, we describe briefly the spectral-analysis procedure, in which the time-series records of the intensity fluctuations are analysed to give the power spectra. This analysis procedure is similar to that described by Rao, Bhandari and Ananthakrishnan (1974), but with some minor modifications. The power spectra are used both to compute the scintillation indices and to determine some of the parameters of the solar wind by the method of model fitting.

3.3.1 Data Reduction

The IPS data reduction is performed off-line, following the completion of the observations. When observing sources at the smaller solar elongations ($\varepsilon \approx 4^\circ - 7^\circ$), the Sun appears in the sidelobes of the beam and causes low-frequency wiggles (frequency $< 0.1\ Hz$) in the records. In order to remove these low-frequency excursions, and also low-level ionospheric scintillation which might be present in the data, the running mean of 10.24-s stretches of data (512 data points) is subtracted from the individual data points. After the running mean subtraction we are left with 2088 data points in each record and only 2048 points are used for the further analysis. Before taking the Fourier transform of 2048 points in a record, the points at the beginning and end of the record are tapered with a cosine weighting function to minimise the effects of data truncation. This tapering causes

a small reduction in the spectral power. Hence, variances are computed before and after the tapering and their ratio is used to correct the final power spectrum.

The Fourier transform is computed using a standard fast Fourier transform algorithm which handles 2^n data points, where n is an integer. The power spectrum is obtained by squaring of the amplitude of the Fourier coefficients. Since the data points are sampled at a rate of 50 Hz, the Fourier transform will contain all frequencies in the range of $\pm 25\ Hz$ and the power spectrum will have a frequency resolution of $50/2048\ Hz \approx 0.025\ Hz$. As the power spectrum is symmetric about zero frequency, we retain only the positive half of the spectrum containing 1024 points in the frequency range 0 to 25 Hz.

Generally, the observations are free of interference. However, if a record is contaminated by interference, as inferred from the simultaneous off-source record, then the whole record of 52-s duration is discarded, even if the interference is present for only part of the time. Typically, we lose 2 – 3 records per hour of observation due to interference. If recurrent interference is present, all data are discarded. After editing out records affected by interference, the individual 52-s power spectra for a given source are co-added to yield a final integrated spectrum of 1024 points, with a frequency resolution of $\approx 0.025\ Hz$.

The integrated power spectrum is corrected for the effect of the receiver time constant by dividing the spectrum by the frequency response of the time constant. The running-mean subtraction performed before taking the Fourier transform acts as a high-pass filter, affecting predominately the low-frequency part of the power spectrum. In effect, the power spectrum is multiplied by a high-pass filter function of the form,

$$HPF = \left[1 - \frac{\sin(\pi f 10.24)}{(\pi f 10.24)}\right]^2 \tag{3.2}$$

All points in the power spectrum, except the first four (at $f \leq 0.1\,Hz$), are corrected for this function by dividing them by eqn. (3.2). The first few points in the spectrum could have been corrupted by wiggles caused by solar disturbances, low-level ionospheric scintillation and slow drifts. Hence, the corrected spectrum is extrapolated for the first four points by fitting a second-degree polynomial to the next forty points of the corrected spectrum.

Fig. 3.1(a) shows a typical IPS power spectrum, corrected for both the high-pass filter function and the effect of the time constant, plotted with a frequency resolution of $\approx 0.025\ Hz$ on a semi-log (log-linear) scale. The scintillating power drops to the mean noise level beyond 5 Hz. Fig. 3.1(b) shows a cold-sky (off-source) power spectrum analysed in the same way. It essentially gives the system-noise power spectrum. The flatness of the off-source spectrum demonstrates that the system noise is white. Semi-log plots are good for visually judging the overall quality of the spectra. However, to see the low-frequency structure of the spectrum to best advantage, it is better to use a log-log plot.

The power spectrum of observed data contains the contribution due to both IPS fluctuations and system noise (compare Figs. 3.1 a and b). The power spectrum of observation $P(f)_{obs}$ can be written as,

$$P(f)_{obs} = P(f)_{scint} + P(f)_{sys} \tag{3.3}$$

The width of the system noise spectrum, $P(f)_{sys}$ is very much greater than that of the IPS fluctuation spectrum $P(f)_{scint}$, being essentially white noise (see Fig. 3.1 b). Hence, $P(f)_{sys}$ is effectively constant with frequency and can be estimated using observations of cold sky. $P(f)_{sys}$ can also be estimated from the on-source scintillation power spectrum. For a typical source observed in the weak-scattering region, the IPS fluctuation spectrum drops to the noise level at frequencies well

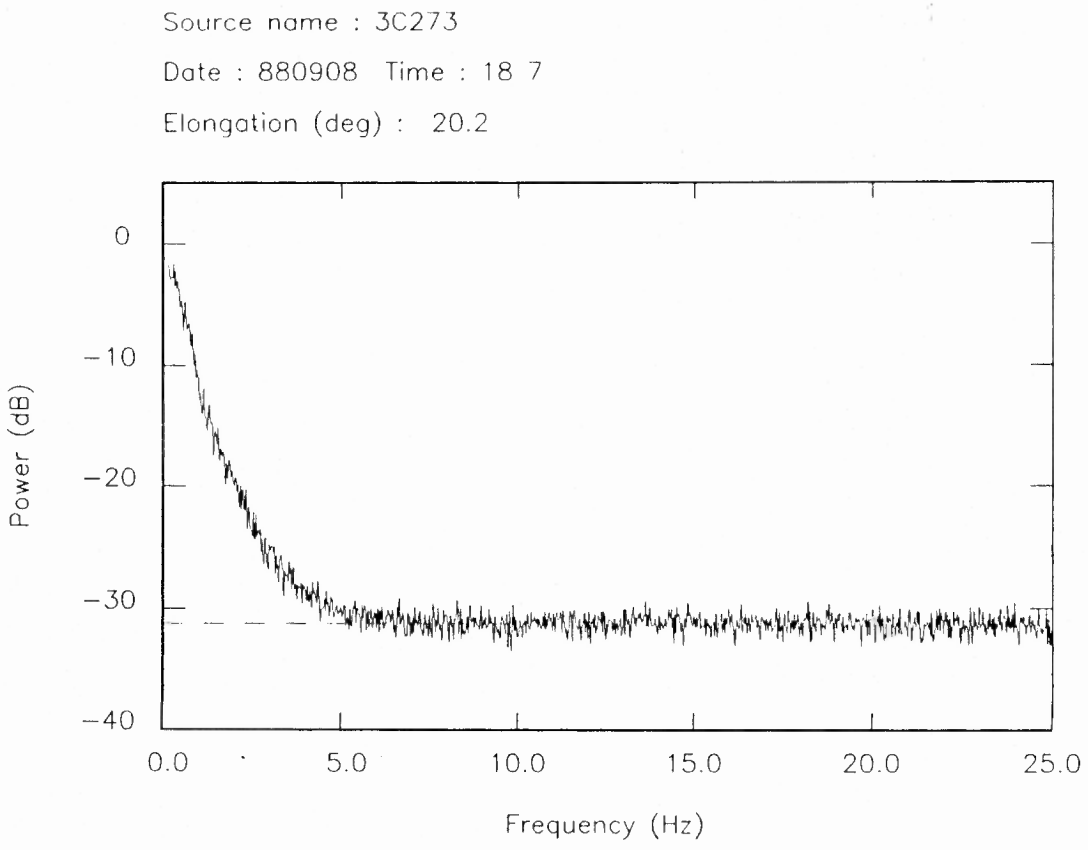

Fig. 3.1(a) A typical IPS power spectrum after correcting for the effect of time constant and high-pass filter function, plotted with a frequency resolution of $\sim 0.025\,Hz$. The horizontal dashed line indicates the constant level caused by the system noise.

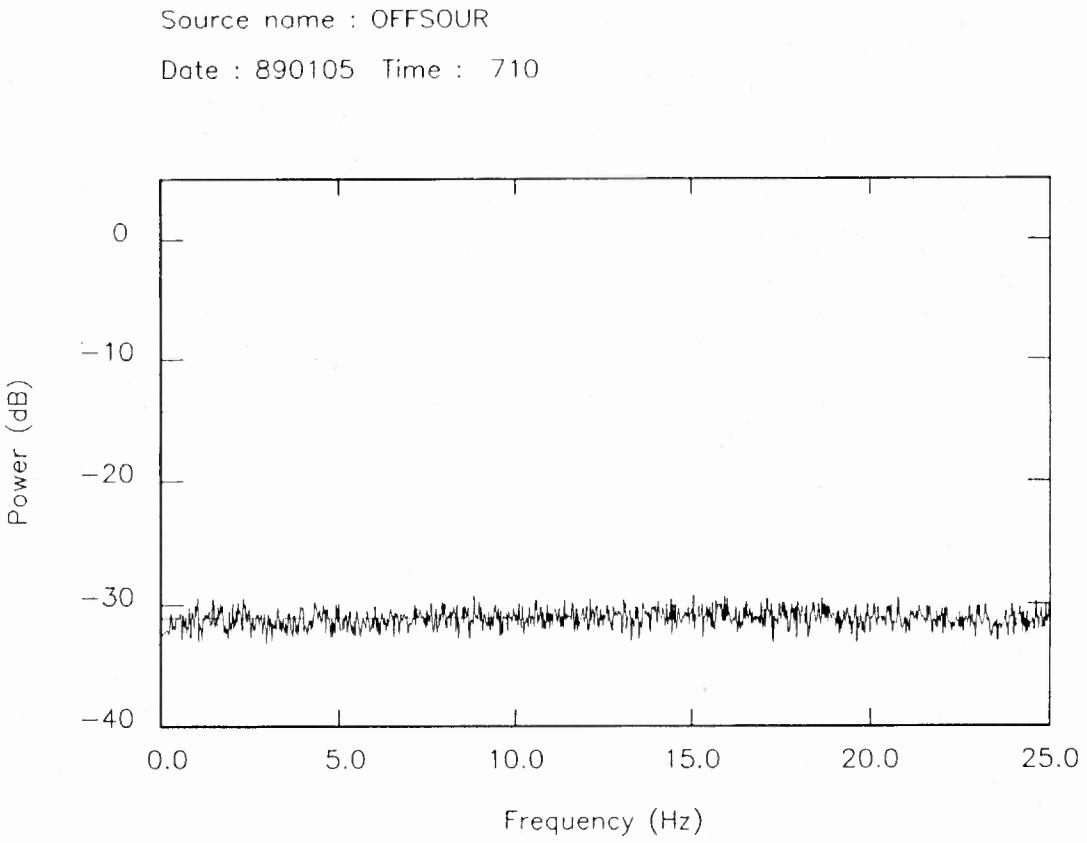

Fig. 3.1(b) The power spectrum of cold sky (off-source) observation.

below 25 Hz, usually by 6 Hz or less. As the system noise is white (Fig. 3.1 b), the on-source power spectrum in the frequency range 12 - 25 Hz can be extrapolated to lower frequencies to provide an estimate of the system noise spectrum and then subtracted from the total power spectrum to give the scintillation spectrum alone. Fig. 3.2 shows a log-log plot of the power spectrum of Fig. 3.1(a) after subtracting the system-noise contribution.

3.3.2 Improvement of Statistical Stability of Spectra

Let us now consider the statistical uncertainty of the estimated power at any particular temporal frequency. It depends on both the power level and the number of power spectra averaged. Following Blackman and Tukey (1959), the fractional uncertainty can be written as,

$$\frac{\delta P(f)}{P(f)_{obs}} \propto (N_{PSM})^{-\frac{1}{2}} \tag{3.4}$$

where N_{PSM} is the number of power spectra averaged. Typically, $N_{PSM} \geq 20$ for our observations. For a given $P(f)_{obs}$, (that is for a particular value of fluctuation power), the fractional error, $\frac{\delta P(f)}{P(f)_{obs}}$, is constant and independent of temporal frequency. However, in the case of the scintillation power spectrum, $P(f)_{scint}$, the signal-to-noise ratio decreases with frequency, since at high frequencies the uncertainty is essentially determined by the system noise power, $P(f)_{sys}$.

Since the scintillation power spectrum $P(f)_{scint}$ and that of the system noise power $P(f)_{sys}$ are uncorrelated, the error $\delta P(f)$ can be obtained by using eqns. (3.3) and (3.4) as,

$$\delta P(f) \propto P(f)_{scint} + P(f)_{sys} \tag{3.5}$$

In this, the system noise spectrum $P(f)_{sys}$ remains constant throughout the spectrum and is independent of the temporal frequency f.

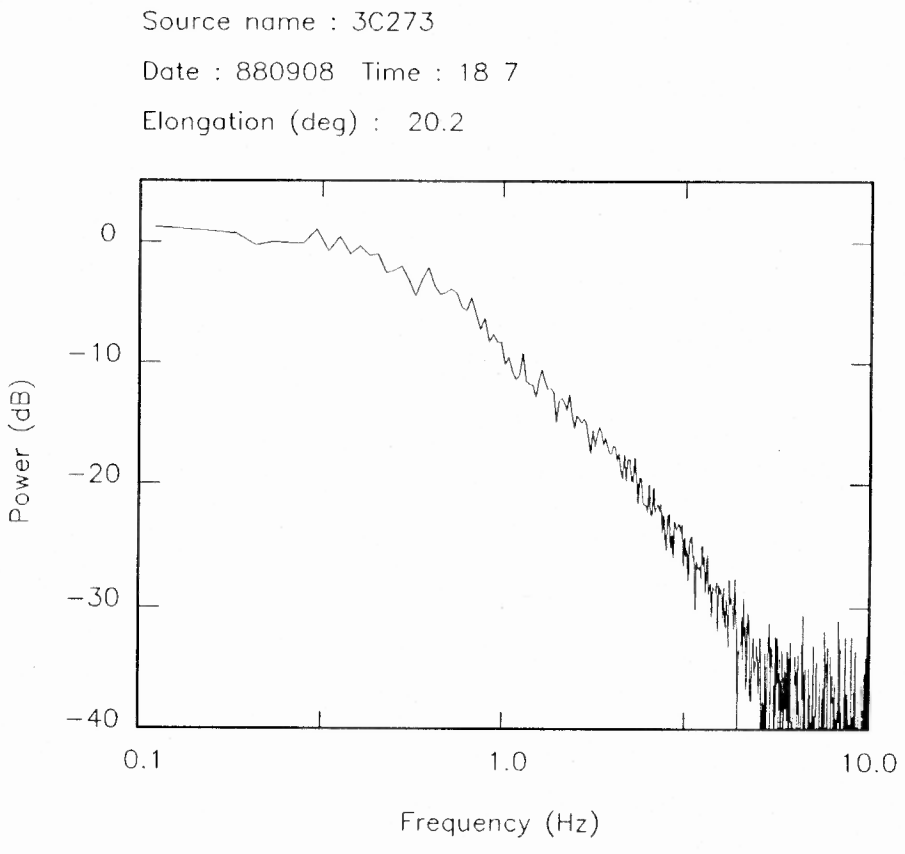

Fig. 3.2 The power spectrum shown in Fig. 3.1(a) is plotted on a log-log scale after subtracting the constant level contribution from the system noise. The frequency resolution $\sim 0.025\,Hz$.

In order to obtain a smoother spectrum, a number of adjacent points can be averaged. However, while averaging, care must be taken not to smear out the Fresnel features in the low-frequency region, as these are essential for performing model fits. If N adjacent spectral points are averaged, then from eqn. (3.4) the uncertainty in the scintillating power alone can be written as,

$$\begin{aligned} \frac{\delta P(f)}{P(f)_{scint}} &= \frac{K}{\sqrt{N}} \left(\frac{P(f)_{obs}}{P(f)_{scint}} \right) \\ &= \frac{K}{\sqrt{N}} \left(\frac{(P(f)_{scint} + P(f)_{sys}}{P(f)_{scint}} \right) \\ &= \frac{K}{\sqrt{N}} \left(1 + \frac{P(f)_{sys}}{P(f)_{scint}} \right) \end{aligned} \tag{3.6}$$

where, for a particular observation, K is a constant whose value depends on N_{PSM}. If the number of points averaged is independent of temporal frequency, we obtain uniform frequency resolution throughout the spectrum. This was the strategy adopted by earlier workers (*e.g.* Rao 1975, Ananthakrishnan 1976).

In such a case, the term $\frac{K}{\sqrt{N}}$ remains constant for all frequencies. Hence, the fractional error of the measured power increases with frequency, especially beyond the cut-off frequency, where the scintillation power is equal the system noise power. This is well illustrated by Fig. 3.2. Hence, it is difficult to obtain reliable information from the high-frequency region of the power spectrum smoothed by the above process. However, high-frequency portion of the spectrum is important for deriving the solar-wind parameters and source-size information. Hence we have used a different method of averaging in order to enhance the statistical stability at high frequencies.

In the present study, the solar-wind parameters are obtained by the method of power-spectrum fitting. For this purpose, we plot the spectrum on a log-log scale, since the power range is very large; of the order of $\approx 10^3 : 1$. In this way, the weak

structures in the spectrum can then be seen clearly. Moreover, the log-log scale is a natural choice since the form of the final spectrum is expected to approximate to a power-law (see Section 2.14). When a spectrum with uniform frequency resolution is plotted on a log-log scale, the separation between spectral points decreases as frequency increases, and points get overplotted in the high-frequency region (see Fig. 3.2).

We see that having high resolution in the high-frequency portion of the spectrum is not useful for the IPS model fitting process. Our requirements are:

1. Sufficient resolution in the low-frequency region ($\sim$ 0.1-Hz resolution around the 1-Hz region).
2. Coarser, but adequate, resolution in the high-frequency region ($\sim$ 1-Hz resolution in the region of 10 Hz).
3. Equispaced spectral points along the log-frequency axis.
4. A uniform statistical stability over the entire usable spectrum.

Therefore, adjacent spectral points should be averaged in such a way as to provide a spectrum distributed uniformly along the log-frequency axis. This will give high resolution at the low-frequency end of the spectrum and lower resolution at the higher frequencies. Item (1) is to ensure that the Fresnel features at the low-frequency portion of the spectra are not smoothed out. Item (2) and (3) are two ensure that unduly nonuniform weightages do not get applied to the different parts of the spectrum during the model fitting process.

To achieve the above requirements, we adopted an averaging method in which the number of points, N averaged at any temporal frequency is directly

proportional to the frequency. That is,

$$N = s \cdot f \tag{3.7}$$

where s is a constant. Thus, the number of spectral points averaged increases linearly with frequency. A smaller value of s gives a higher frequency resolution at any particular frequency. Fig. 3.3 shows for our spectra, the plot of the number of points averaged as a function of temporal frequency. It may be noted that approximately 5 points are averaged per Hz. Thus, around the 10-Hz region, nearly 50 points are averaged to obtain the spectral point. This averaging gives :

1. A resolution of $\approx 0.1\,Hz$ at a frequency of 1 Hz.
2. A resolution of $\approx 1\,Hz$ at 10 Hz.
3. A final spectrum containing just 40 points distributed uniformly along the log-frequency axis.
4. The fractional error up to the cut-off frequency (where the power drops to the noise level) remains approximately constant.

We will refer to this averaging method as the method of uniform statistical (or uniform error) averaging.

Let us now consider the fractional error at different temporal frequencies in the case of the averaging described by eqn. (3.7). Substituting eqn. (3.7) into (3.6), we can obtain the fractional error in terms of frequency, instead of N. Consider a scintillation source power spectrum with good signal-to-noise ratio. Then, for the spectral region around 1 Hz, the scintillation power, $P(f)_{scint}$, is much larger than the system-noise contribution, $P(f)_{sys}$ (see Fig. 3.1 a) and the fractional error of the scintillation power is approximately $\frac{K}{\sqrt{S}}$. For such a source in the weak-scintillation regime, the power drops to the noise level around 5 Hz.

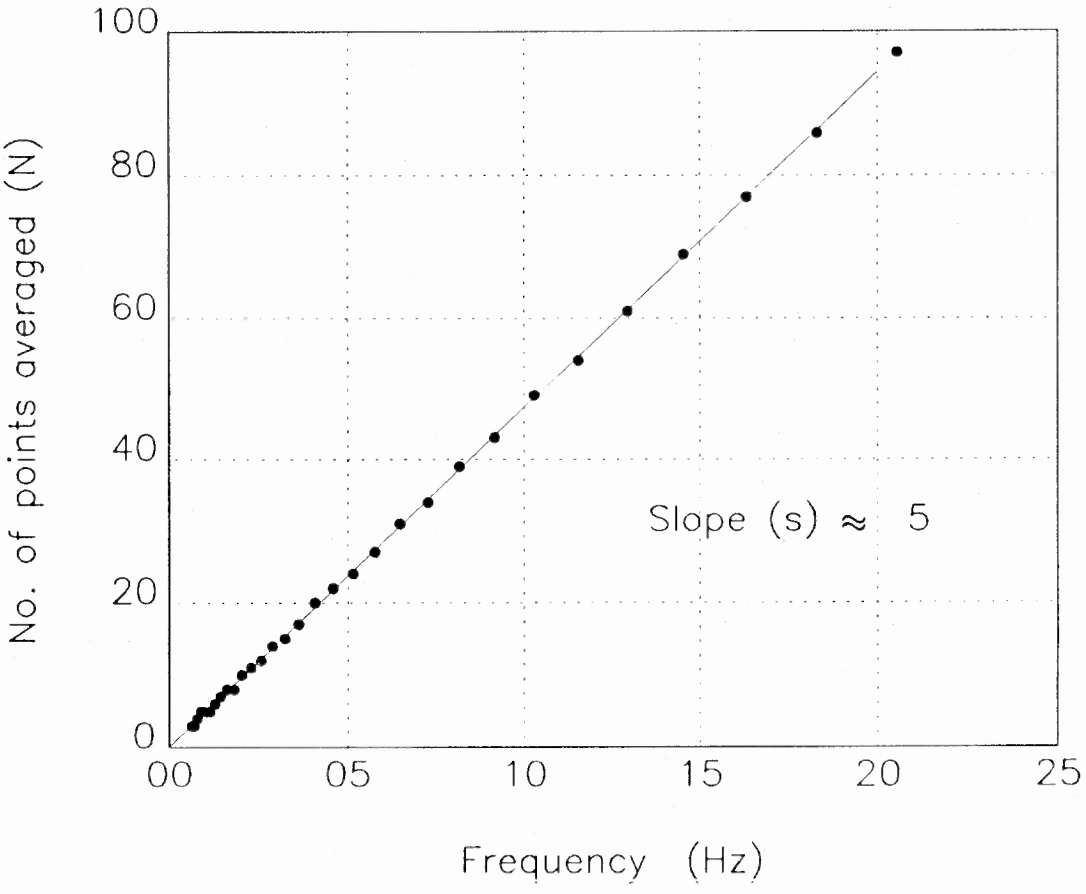

Fig. 3.3 Graph showing the number of points averaged at different temporal frequencies. Number of points averaged increases with temporal frequency, giving 0.1 Hz resolution at low-frequency region (1 Hz region) and 1 Hz resolution at the high-frequency region (10 Hz region).

At the frequency where $P(f)_{scint} \geq P(f)_{sys}$, which occurs just below the cut-off frequency, *i.e.* at around 4 Hz, where the fractional error still approximates to $\frac{K}{\sqrt{S}}$. Hence, we see that the fractional error over the usable region of the spectrum remains practically constant using this method of uniform statistical averaging.

Summarising, if we maintain the same frequency resolution over the entire spectrum, then the fractional error will grow steadily with frequency and thus the high-frequency portion of the spectrum will be unusable. Fig. 3.4 shows the plot of percentage error against temporal frequency for the cases of fixed four-point averaging and uniform statistical averaging for the spectrum shown in Fig. 3.2. It is clear that for the fixed-point averaging (shown by filled circles), the percentage error increases monotonically with frequency. However, in the case of uniform statistical averaging (open circles), the percentage error remains practically constant up to the cut-off frequency.

In Fig. 3.5, we present the log-log plot of the power spectrum shown in Figs. 3.1(a) and 3.2, after applying the uniform statistical averaging described above. Comparison with the spectrum having uniform resolution, in Fig. 3.2, shows that the spectrum in Fig. 3.5 is much less noisy; yet the Fresnel features are retained. For spectra subjected to the fixed point averaging, noise overwhelms signal at regions close to the cut-off frequency. In effect, the method of uniform statistical averaging used by us increases the signal-to-noise ratio of the power spectrum in its high-frequency portion.

3.3.3 The Scintillation index

The r.m.s of the intensity fluctuations due to IPS is equal to square root of the area under the power spectrum (see Section 2.4). Hence, the scintillation

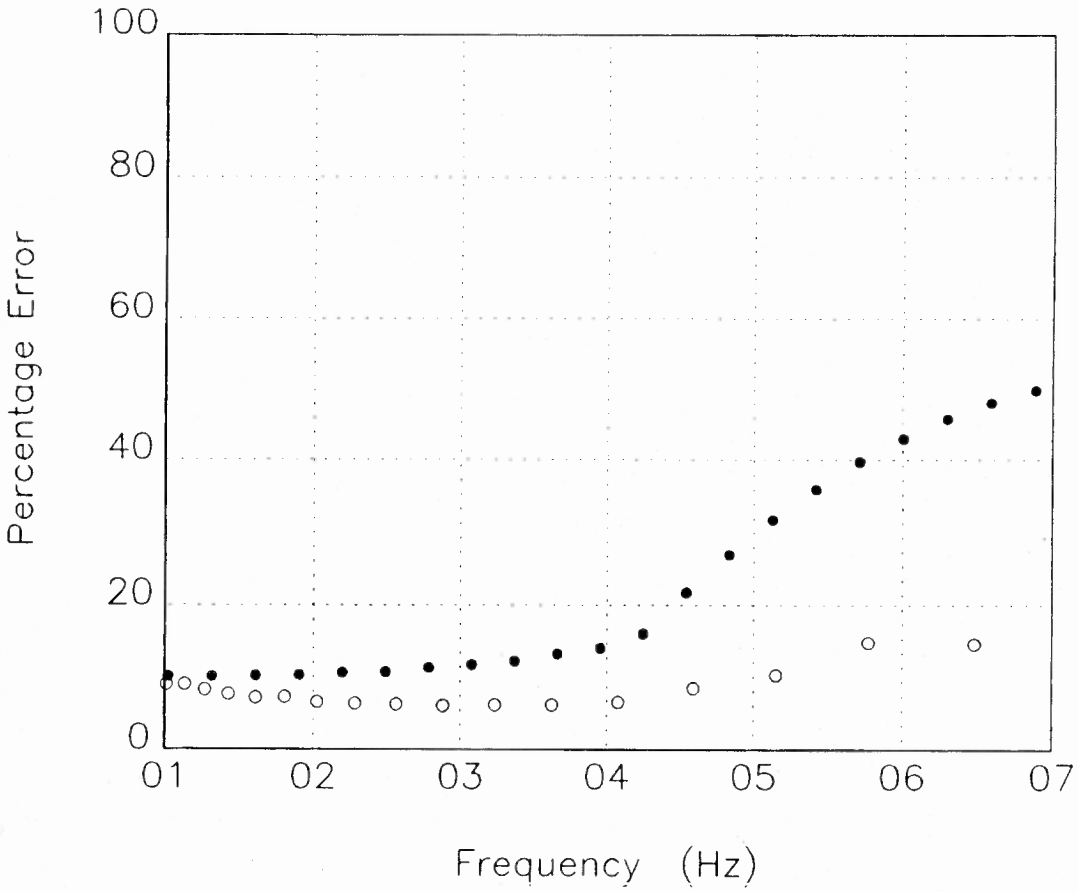

Fig. 3.4 The percentage error at different temporal frequencies of the power spectrum for the four-point averaging (*filled circle*) and uniform statistical averaging (*open circle*).

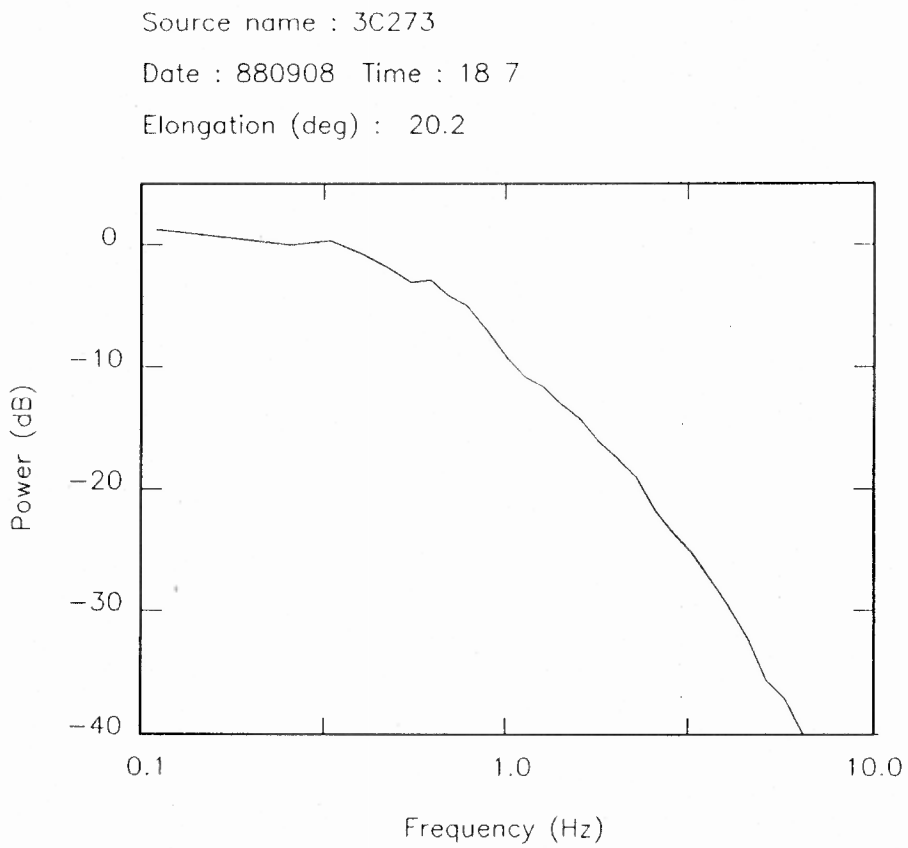

Fig. 3.5 The power spectrum shown in Figs. 3.1(a) and (3.2), after applying the method of uniform statistical averaging.

index is computed using the following relation,

$$m^2 = \int_0^{f_c} P(f)_{scint}\ df\ /\ < I >^2 \tag{3.8}$$

where $P(f)_{scint}$ is the scintillating power, f_c the cut-off frequency of the power spectrum where the scintillating power equals the noise level and $< I >$ the mean source intensity. The mean source intensity can be estimated from the on- and off-source data, as described in Section 3.2.

The scintillation indices estimated for PKS 1148–001 from observations during the years 1986 – 89 are shown in Fig. 3.6 (a)-(d) plotted against solar elongation angle, ε (see the IPS geometry in Fig. 2.2). Far from the Sun, the scintillation index, m, increases with decreasing perpendicular distance, p, between the Sun and the line-of-sight to the source. It reaches a maximum at p_{peak} ($\approx 45\,R_o$ for our observing frequency). Thereafter, for $p < p_{peak}$, m decreases with decreasing p. For $p > p_{peak}$ we observe weak-scattering, while for $p < p_{peak}$ we are in the strong-scattering regime. For PKS 1148-001, the maximum value of scintillation index reaches almost unity around p_{peak} and hence the source has almost all its flux density in the scintillating component (Venugopal *et al.* 1985). This compact source has been observed regularly at Ooty since 1976 and has been used as the IPS calibrator for all our observations. Our scintillation-index measurements and their interpretation are presented in Chapter 5 of this thesis.

3.4 The Model Power Spectrum

The principal objective of the present study is to investigate the method of model power-spectrum fitting and how this can be used to estimate the parameters of the solar wind from single-station IPS observations. Therefore, it is instructive to examine changes in the shape of the theoretical model power spectrum for changes

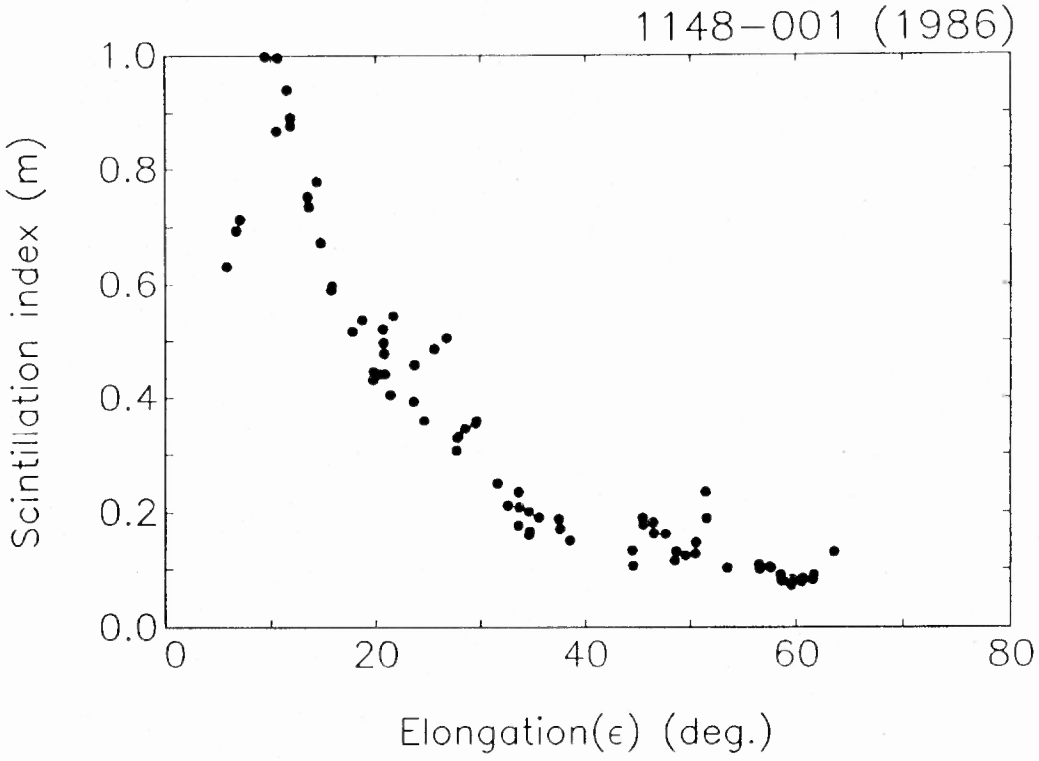

Fig. 3.6(a) Scintillation index, m, of the compact source $PKS1148\text{-}001$, plotted as a function of solar elongation, ε, for the year 1986.

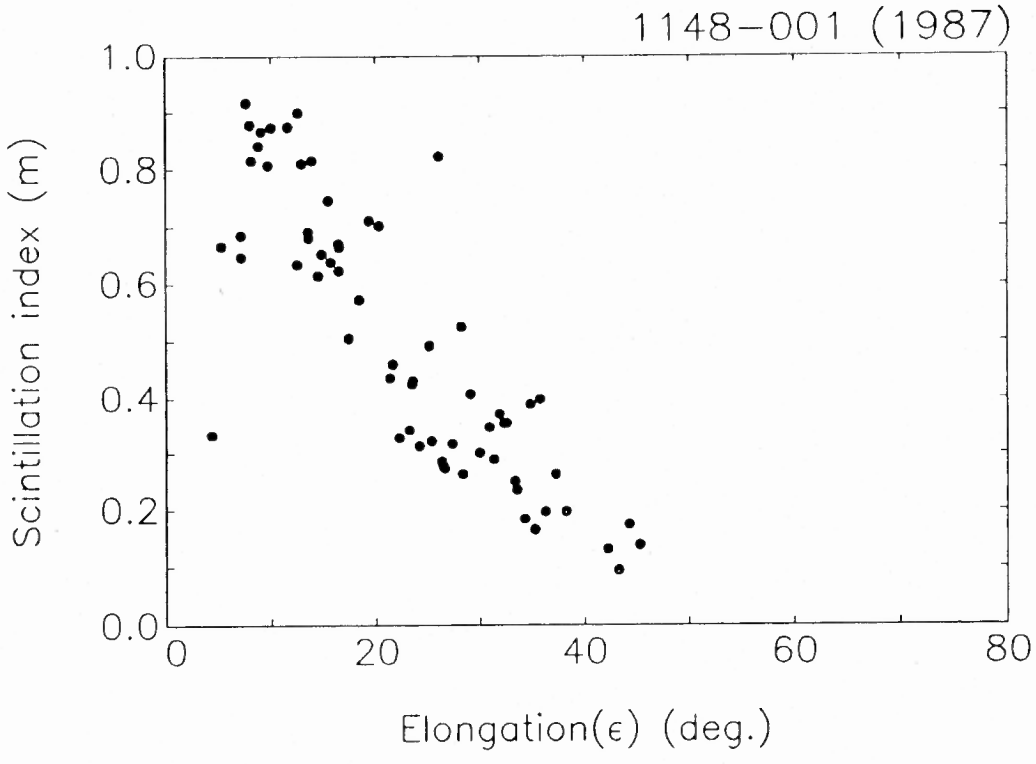

Fig. 3.6(b) Same as Fig. 3.6(a), for the year 1987.

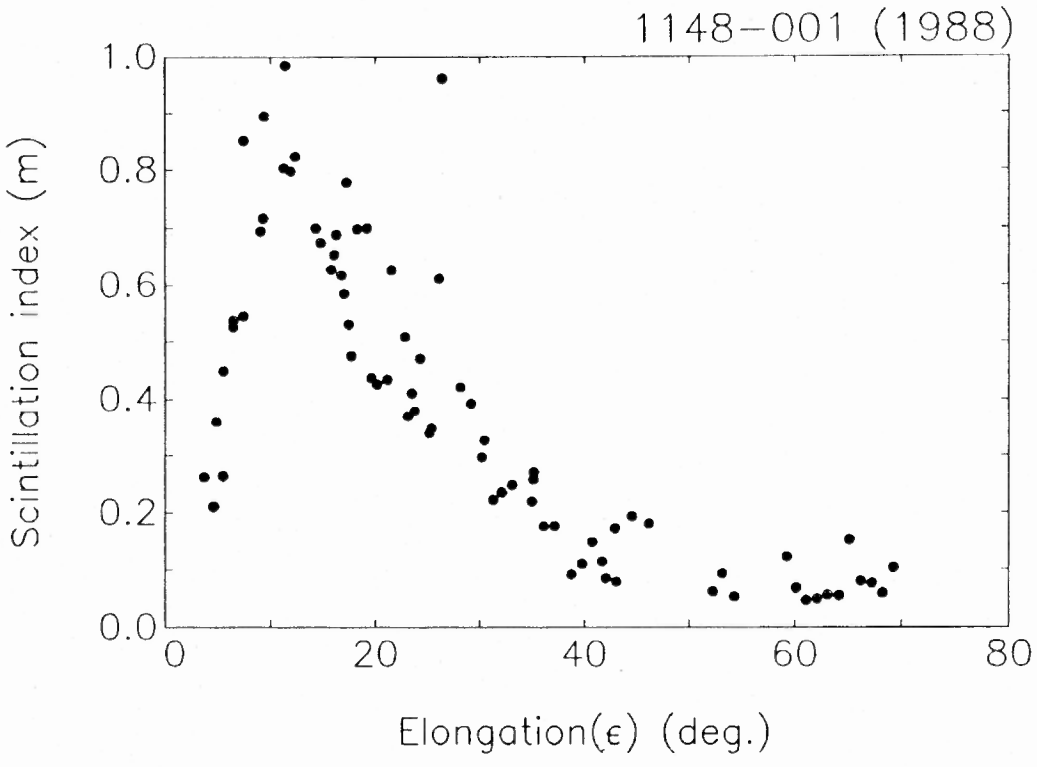

Fig. 3.6(c) Same as Fig .3.6(a), for the year 1988.

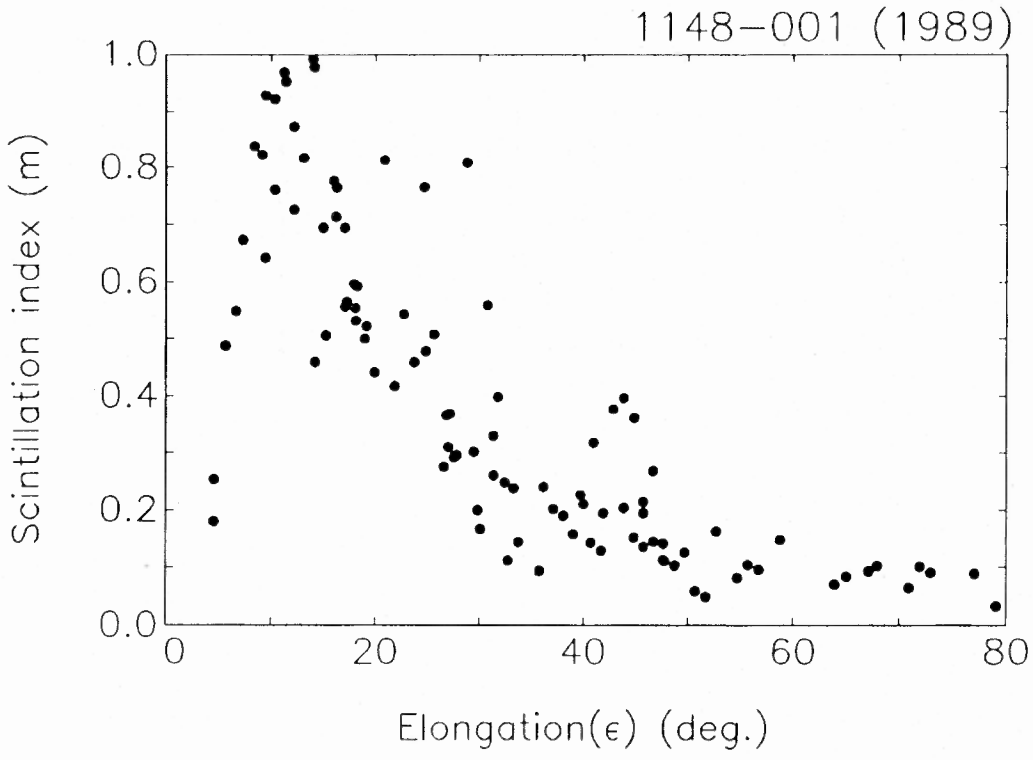

Fig. 3.6(d) Same as Fig. 3.6(a), for the year 1989.

in the various parameters of the solar wind. The relevant scintillation theory for the weak-scattering case has been discussed in Chapter 2, in which it has been shown that the observed intensity is directly related to the electron-density spectrum of the medium. Therefore, the shape of the intensity spectrum in the weak-scattering region is determined by the electron-density spectrum (see eqn. 2.83). However, the Fresnel propagation filter, the velocity distribution, and the source visibility function also modify the shape of the observed spectrum. In the following sections, we discuss the model power spectrum and its sensitivity to the parameters.

3.4.1 The Model Parameters

The form of the electron-density fluctuation spectrum derived from various experiments predicts that the IPS power spectrum should be a power-law (see Section 2.14). This can be seen clearly from the portion of the spectrum at high temporal-frequencies (the low-frequency portion is heavily attenuated by the Fresnel filter function; see Section 2.14 and Fig. 2.5). Further, our present observations (Section 5.5), earlier IPS measurements (Readhead 1971, Rao, Bhandari & Ananthakrishnan 1974, Coles 1978, Armstrong & Coles 1978) and spacecraft experiments (Woo & Armstrong 1979) provide a model for the scattering power, or turbulence strength, as a function of radial distance from the Sun which approximates to a simple power-law of the form $R^{-\beta}$. Thus, for a source of finite size, the scintillation power spectrum has the form of eqn. (2.83),

$$P(f) = (2\pi r_e \lambda)^2 \int_{-\infty}^{Z} \frac{dz}{|V_p(z)|} \int_{-\infty}^{\infty} dq_y 4 \sin^2(q^2 z/2k) |V(q, z, \theta_\circ)|^2 R^{-\beta} q^{-\alpha} \qquad (3.9)$$

where f is the temporal frequency, r_e the classical electron radius, $\lambda = 2\pi/k$ the wavelength of observation, Z the distance from the Earth to the closest approach of the line-of-sight to the Sun, $V_p(z)$ the radial velocity component projected on

the x, y plane ($= 2\pi f/q_x$), z the distance to the screen, $q = (q_x^2 + q_y^2)^{\frac{1}{2}}$ the spatial wavenumber, R the distance between the Sun and the screen situated along the line-of-sight (*i.e.* the heliocentric distance to the layer), and $|V(q, z, \theta_\circ)|$ the source visibility function.

We see from eqn. (3.9) that an IPS model spectrum is a function of observing wavelength λ, the propagation path length z, the strength of turbulence $R^{-\beta}$, the slope of the assumed power-law turbulence spectrum α, the solar-wind velocity $V_p(z)$ and the source size $\theta_\circ$. The computation of the model spectrum should be performed by integrating through the extended medium along the line-of-sight, employing the weak-scattering approximation.

3.4.2 The Geometrical Velocity Projection

The spatial diffraction pattern (produced by the interplanetary medium), is converted into an observed time series of source intensity by the motion of the irregularities at the velocity of the solar-wind. To compute the model power spectrum of the IPS, we must consider the rate at which the medium moves across the line-of-sight from layer to layer, even if we were to assume a constant solar-wind velocity. This is necessary owing to the geometrical projection effect. Thus, since $q_x = 2\pi f/V_p(z)$, different values of spatial frequency q, contribute to a given temporal frequency f, for different points along the line-of-sight and the projected velocity changes from layer to layer. We predict the projected transverse velocity from simple trigonometry. Further, the projected velocity along the direction perpendicular to the line-of-sight is weighted by the Fresnel filter $\sin(q^2 z/2k)$, the source-size filter of $|V(q, z, \theta_\circ)|^2$ for a finite-sized source, the local level of turbulence $R^{-\beta}$ and the electron-density turbulence spectrum $q^{-\alpha}$. While model fitting, if this projection effect is not considered it can result in underestimation of the

velocity of the solar wind by 15 – 20 %, for a spherically-symmetric distribution of the solar wind (see Section 4.7).

3.4.3 The Line-of-sight Weighting Function

Our analysis of scintillation indices (see Section 5.5), other IPS observations at various frequencies (Readhead 1971, Rao, Bhandari & Ananthakrishnan 1974, Coles 1978, Armstrong & Coles 1978) and spacecraft experiments (Woo & Armstrong 1979) show that the scattering power in the solar wind varies as R^{-4} (*i.e.* $\beta \approx 4$). Therefore, for a spherically-symmetric solar-wind distribution, layers at different distances from the Sun have different scattering powers. The IPS observed at a point on the Earth is the integrated effect of the IP medium along the line-of-sight. Fig. 3.7 (a) shows the scattering-power weighting functions, computed using eqn. (2.48), for the case of an ideal point source, as a function of line-of-sight distance, z, for various solar elongations (see Fig. 2.2). These are computed for 327-MHz observations with the assumptions of a spherically-symmetric solar wind and a power-law electron-density spectrum, $\Phi_{\Delta N_e}(q) \propto R^{-4}\, q^{-3.3}$. The vertical dashed lines on the plots indicate the position of closest solar approach for the line-of-sight path. It is evident from the figure that the main contribution to the scintillation comes from the layers near the point of closest approach. As the source moves closer to the Sun, a major part of the scattering occurs in a thin layer of the medium. However, when the source is at a large distance from the Sun ($\varepsilon \approx 60°$), the weighting function broadens and hence the medium must be treated as an extended diffracting screen.

Figs. 3.7 (b) and (c) show the scattering-power functions computed for source sizes of 100 and 200 *mas* respectively. In these plots, we have normalised

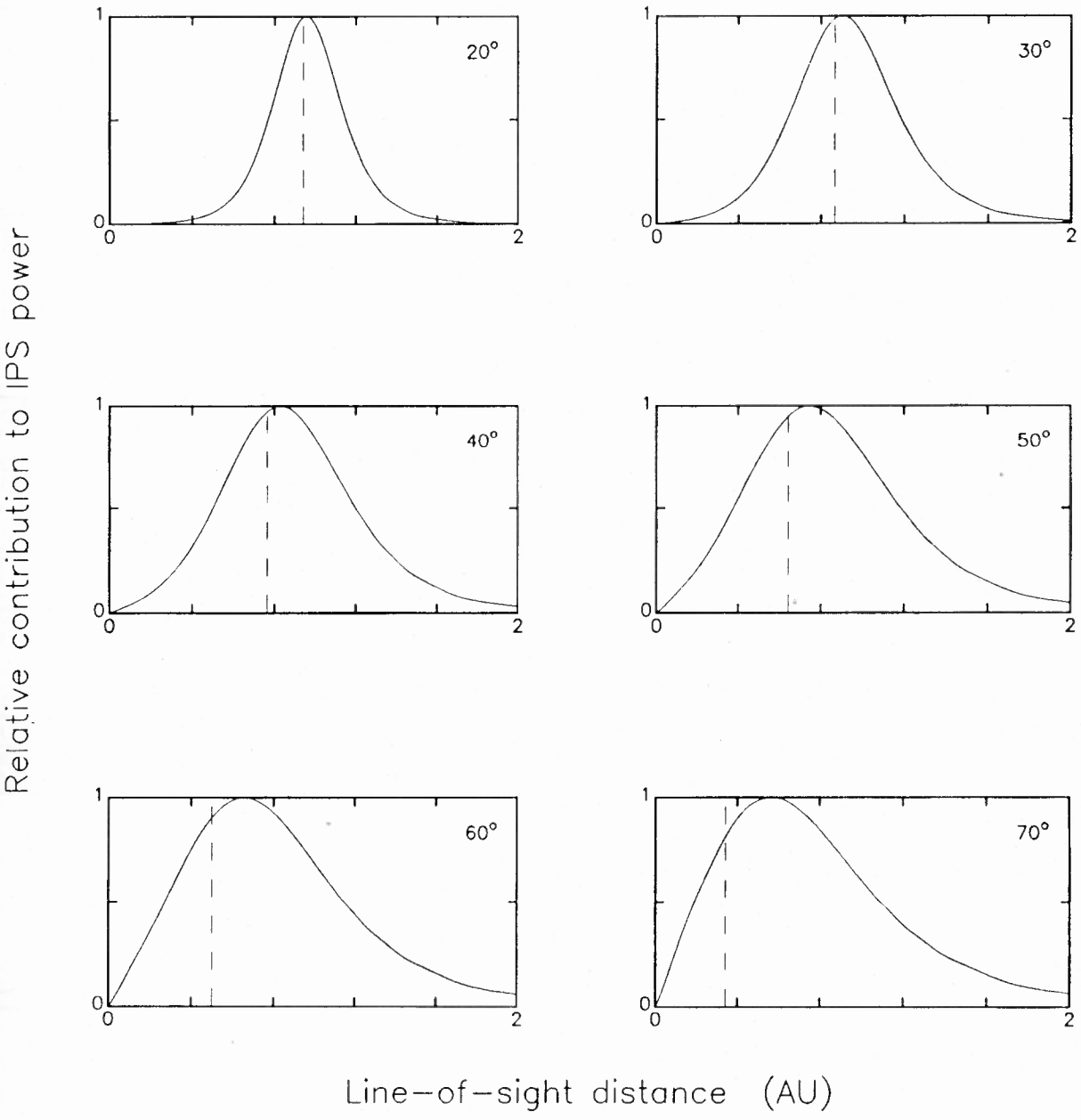

Fig. 3.7(a) Computed IPS weighting functions along the line-of-sight, at the solar elongation angles indicated. A power-law density fluctuation spectrum $\Phi_{\Delta N_e}(q) \propto R^{-4} q^{-3.3}$ is assumed. An ideal point source is also assumed. The vertical dashed line indicates the point of closest approach on the line of sight.

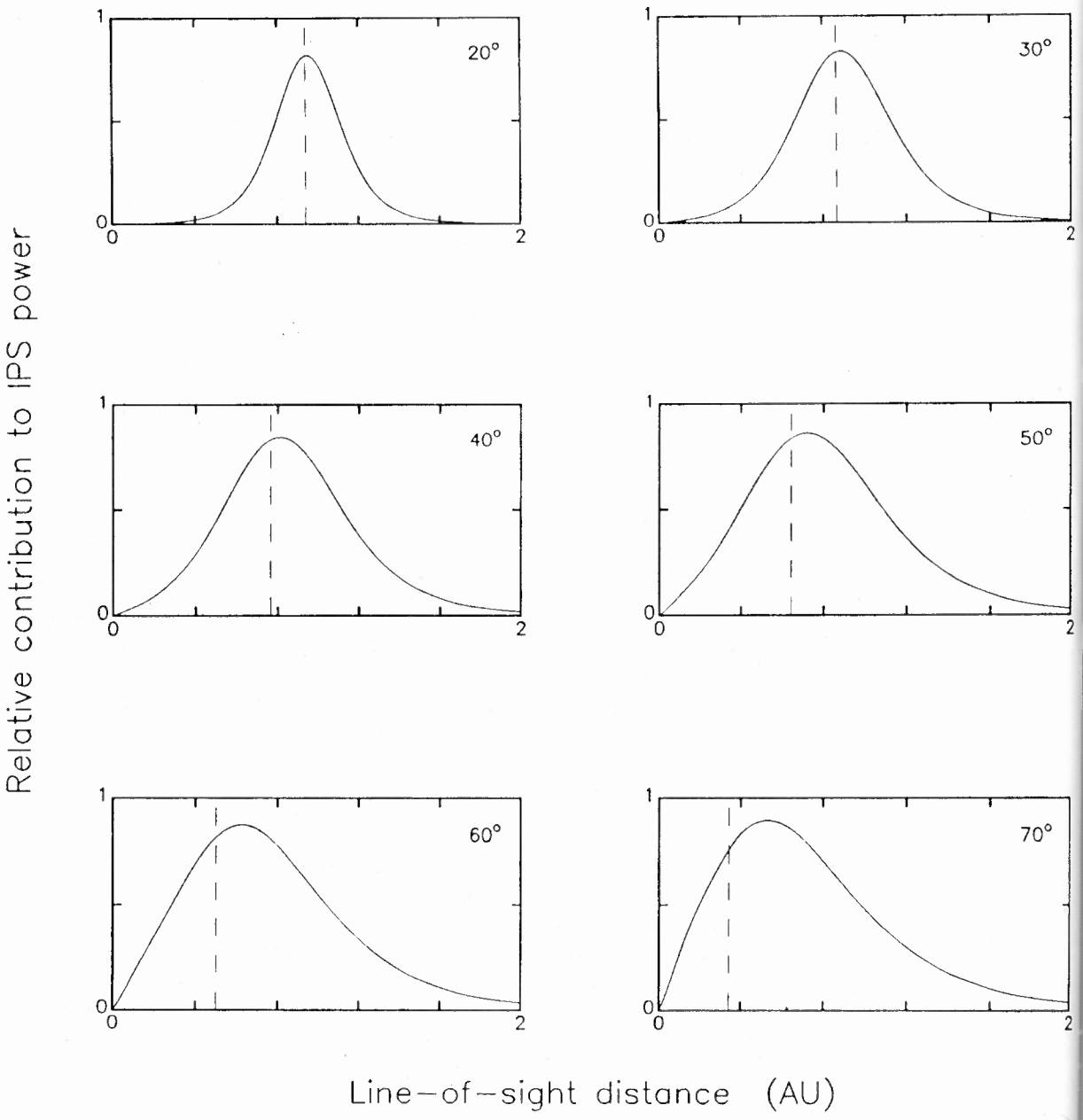

Fig. 3.7(b) Same as Fig. 3.7(a), for the source size, $\Theta_S = 100\,mas$.

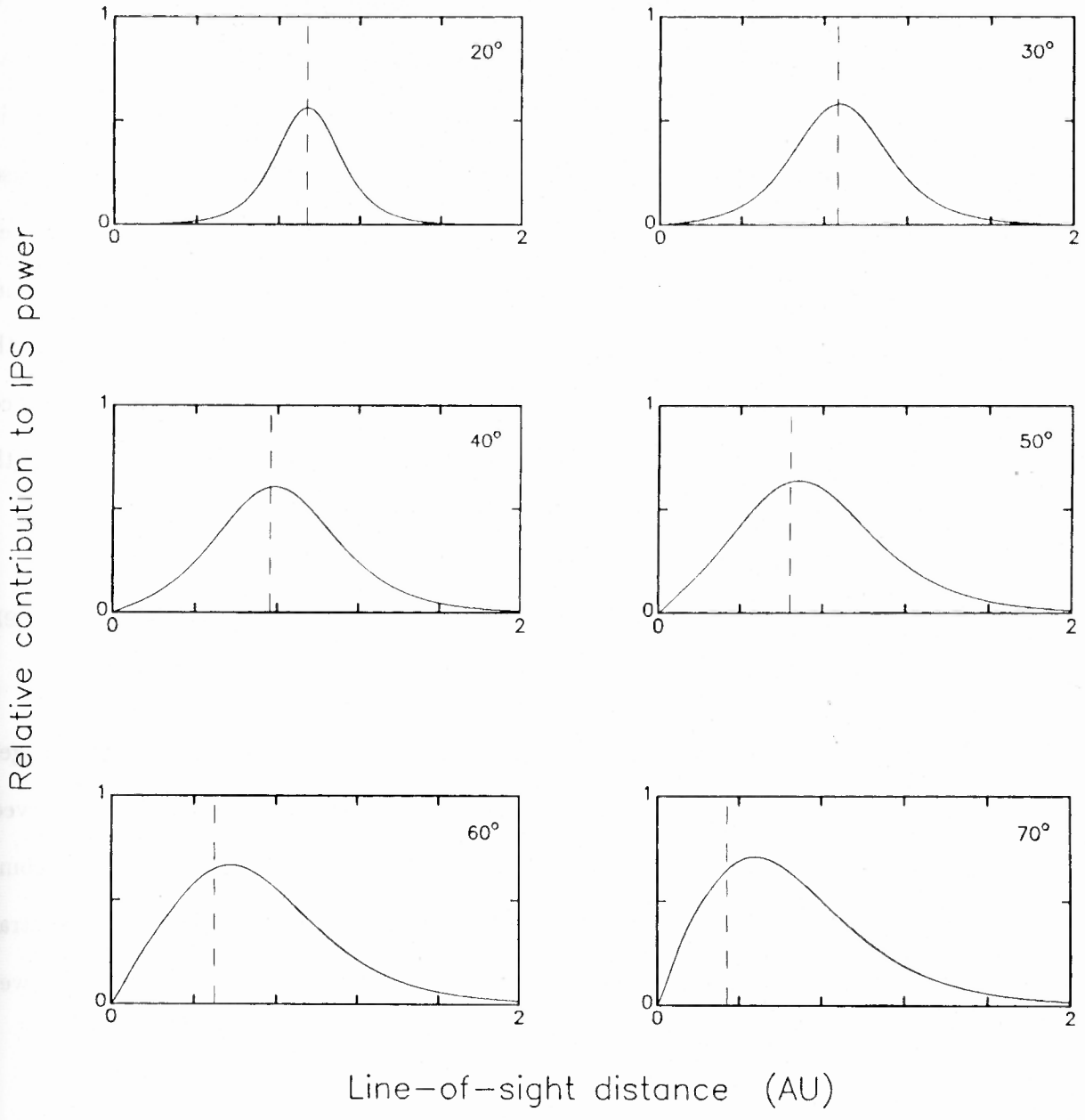

Fig. 3.7(c) Same as Fig. 3.7(a), for the source size, $\Theta_S = 200\,mas$.

the scattering power with respect to that at the maximum for the ideal-point-source scattering power given in Fig. 3.7 (a). From Figs. 3.7 (a) - (c), we note that the overall shape of the weighting function at a given elongation is similar for different source sizes. However, it is also seen that the scattering power is reduced by the source-size filter, being scaled upward or downward for a decrease or increase of source size. Further, these results show that the scattering power for various solar elongations, decreases beyond the point of closest approach and falls practically to zero around $z = 2\,AU$, where z is the distance from the Earth along the line-of-sight. Hence, the integration in eqn. (3.9) is cut off at a distance $2\,AU$ from the Earth. The integrals are evaluated numerically with a step length of $\Delta z \approx 0.05\,AU$.

3.4.4 The Effect of Solar-Wind Parameters on the Power Spectrum

In order to understand how the shape of the IPS power spectrum changes with solar-wind parameters, we start by considering an ideal-point-source observed through a uniform spherically-symmetric solar-wind. The model spectra are computed using eqn. (3.9). For the comparison of changes in shape of the spectra, with the parameters of the solar wind, they are normalised to an arbitrary power level and plotted on a log-log scale.

(a) The Power-law Index

The effect of varying the power-law index α on the shape of the spectrum due to an ideal point source is shown in Fig. 3.8 for a solar wind with constant radial velocity of 400 kms^{-1} and at a solar elongation of $\varepsilon = 20°$. In the log-log plot of Fig. 3.8, a power law will be a straight line. We see from the figure that the

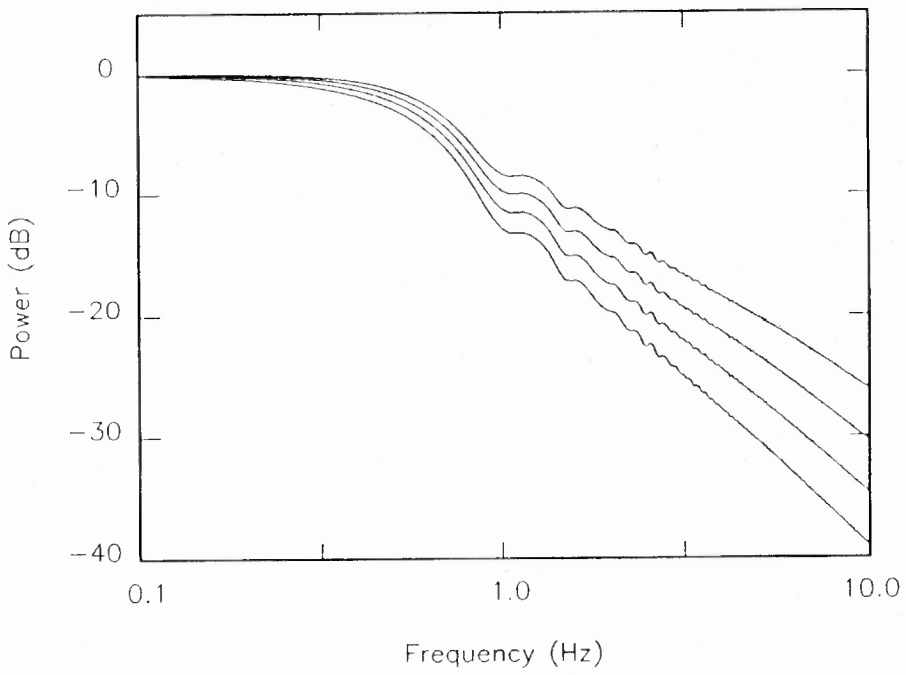

Fig. 3.8 Point source model spectra showing the effect of power-law index, α. The power-law index $\alpha = 3.0$ for the top spectrum and increases by 0.3 for each subsequent spectrum to a value $\alpha = 3.9$ for the bottom spectrum. The spectra have been computed for the solar elongation $\varepsilon = 20°$ with a velocity 400 kms^{-1}.

spectrum becomes steeper in the high-frequency portion as the power-law index α is increased. This means that the scattering power falls off more rapidly with temporal frequency for a medium with a higher value of α.

In general, the power spectrum for an ideal point source has a flat portion at low frequencies, $f < f_f$, caused by the Fresnel-filter function acting on the power-law shape of the spectrum. (The Fresnel-filter function attenuates the low frequencies and acts as a high-pass filter.) Around the frequency f_f, a transition region occurs corresponding to the first minimum of the Fresnel-filter function (see Fig. 2.3). This is called the "*Fresnel knee*". The other oscillations caused by the Fresnel filter are smeared out by the integration along the line-of-sight. For frequencies $f > f_f$, the spectrum has a power-law form, appearing as a straight line on the log-log plot with a slope of $(-\alpha + 1)$. The slope is increased by one because of the strip integration performed over the spatial coordinate q_y. We note that from observations of an ideal point source, it is possible to obtain the power-law index from the observed temporal spectrum at frequencies $f > f_f$, if no other properties of the solar wind were to affect the spectrum at high frequencies.

(b) The Solar-Wind Velocity

In Fig. 3.8, we note that changes in the power-law index over the expected range of 3.0 to 3.9 do not affect the frequency of the Fresnel knee to any large extent. The residual effect is that the knee moves inward or outward slightly depending on the increase or decrease of the power-law index α. Of much more significance, the frequency of the Fresnel knee, f_f, is proportional to the velocity of the solar-wind. This is because the temporal power spectrum as a function of

frequency f is related to the spatial wave number q_x by

$$q_x = \frac{2\pi f}{V_p(z)} \tag{3.10}$$

where $V_p(z)$ is the projected solar-wind velocity, at a screen distance z, along the x-direction perpendicular to the line-of-sight. Hence, a change in velocity scales the spectrum in frequency and the whole spectrum contracts or expands depending on whether the velocity decreases or increases.

Fig. 3.9 shows the effect of a change of velocity on the power spectrum of an ideal point source for power-law index $\alpha = 3.3$ and solar elongation $\varepsilon = 20°$, plotted on a log-log scale. A log-log plot is well suited to this case also, as it allows the determination of the solar-wind velocity by simply sliding a template power spectrum along the frequency axis. A spectrum showing a sharp Fresnel knee, with an identifiable Fresnel first minimum, makes it simple to obtain an accurate value for the solar-wind velocity.

(c) The Axial-Ratio

Multi-station IPS observations (Blessing & Dennison 1972, Coles & Kaufman 1978, Scott, Coles & Bourgois 1983 and Kojima 1979) show that the irregularity pattern is not isotropic, but that the irregularities in the solar wind which give rise to scintillations appear to be elongated along the interplanetary magnetic-field lines or the solar-wind velocity. The spatial structure of the intensity pattern can be approximated by a characteristic ellipse, with the pattern aligned in the direction radial from the Sun. The ratio of the major to minor axis, AR, is called the axial ratio. If $AR = 1$, the pattern is said to be isotropic, while for other values of AR the pattern is referred to as anisotropic. In the present work, we have included

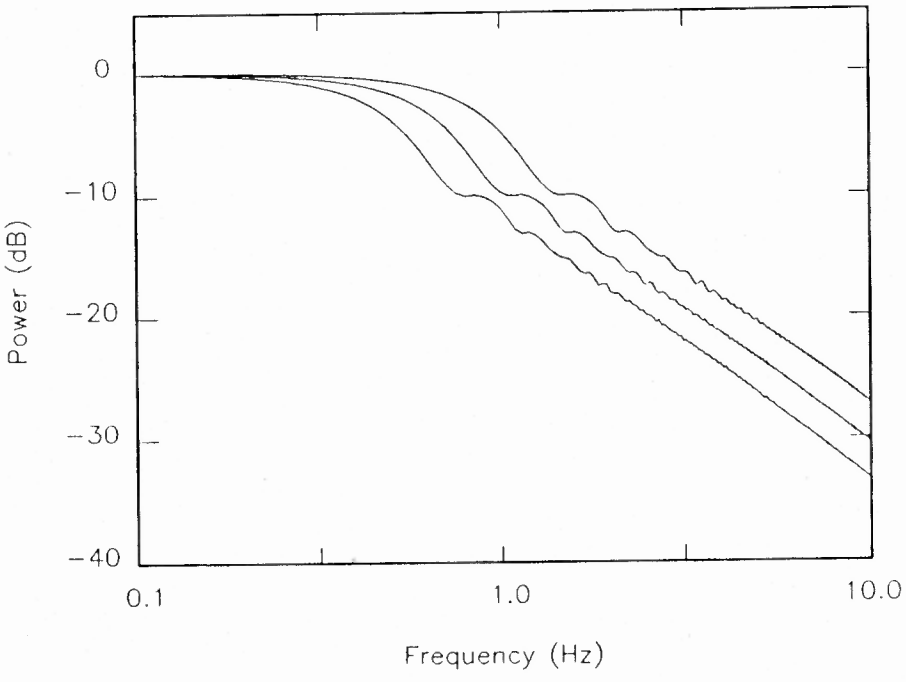

Fig. 3.9 Point source model spectra showing the effect of solar-wind velocity. The velocity $V = 300\,kms^{-1}$ for the bottom spectrum, $V = 400\,kms^{-1}$ for the middle spectrum and $V = 550\,kms^{-1}$ for the top spectrum. The spectra have been computed for solar elongation $\epsilon = 20°$ with a power-law index $\alpha = 3.3$.

the effect of the anisotropic medium in the computation of the model spectrum by setting,

$$\Phi_{\Delta N_e}(q) \propto \left(q_x^2 + \frac{q_y^2}{AR^2} \right)^{-\alpha/2} \tag{3.11}$$

However, in the weak-scattering region ($R > 40\,R_\odot$) the pattern is essentially isotropic (Coles & Kaufman (1978).

Fig. 3.10 shows the effect of anisotropy on the point-source power spectrum for a solar-wind velocity of 400 kms^{-1}, power-law index of $\alpha = 3.3$ and a solar elongation of $\varepsilon = 20°$. We note that as the axial ratio increases, the Fresnel knee caused by the Fresnel-filter first minimum becomes increasingly rounded (or blunt), and Fresnel oscillations are smeared out. In our weak-scattering scintillation observations, an axial ratio of $AR > 1$ may not be required, except for the regions closest to the Sun, around 40 to 60 $R_\odot$. Should the brightness distribution of the source be asymmetric, this will also produce a similar effect to an anisotropic medium. Therefore, for an asymmetric source, the detailed brightness distribution has to be considered while model fitting.

(d) The Random Velocity

In any general model for computing theoretical power spectra, we should include integration over a range of velocities, in addition to the effects of velocity projection due to the geometry of the uniform spherically-symmetric solar wind. The presence of a range of velocities in the solar wind (random velocity components) makes a considerable contribution to the scintillation. Such velocity spreads may be due to the physical nature of the scattering medium and can be expressed as a probability distribution of velocity in the x, y plane which weights each screen for the different velocities. Thus, the effect of random velocities on the temporal

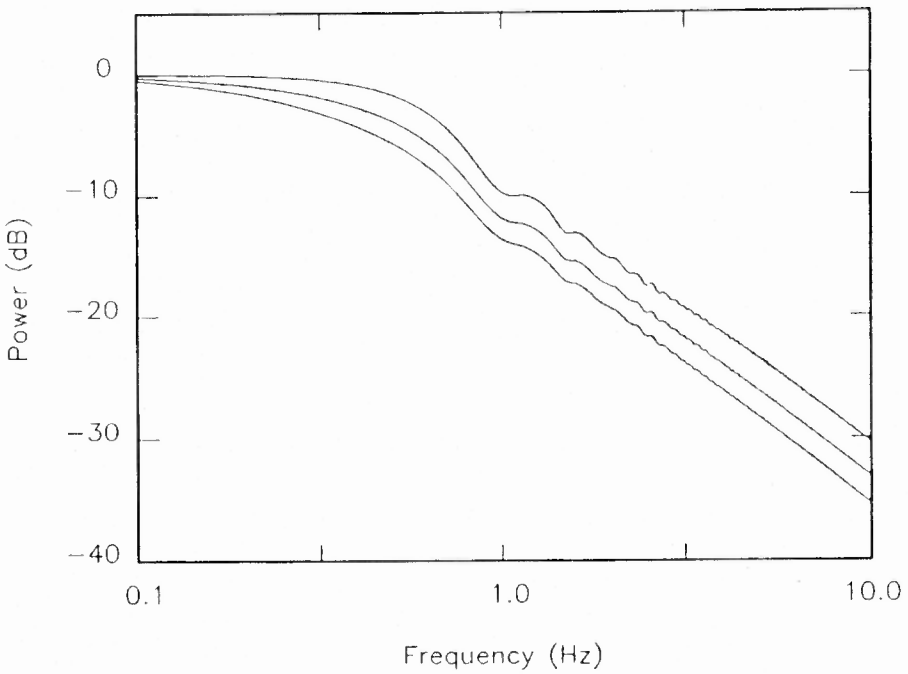

Fig. 3.10 Point source model spectra showing the effect of axial ratio. The axial ratio of the medium, $AR = 1.0$ for the top spectrum, $AR = 1.3$ for the middle spectrum and $AR = 1.6$ for the bottom spectrum. The spectra have been computed for the solar elongation $\varepsilon = 20°$ with power-law index $\alpha = 3.3$.

spectrum is analogous to the influence of the extended medium. Further, the random velocity component affects the power spectrum in a similar manner to the axial-ratio effect. A random velocity spread of $\frac{\Delta V}{V} \approx 25$ % rounds (or blunts) the Fresnel knee of the power spectrum in a similar way to an axial ratio of $AR = 1.1$. However, a non-turbulent solar-wind model, in the form of a uniform, spherically-symmetric solar wind is satisfactory for observations at distances greater than 30 $R_\circ$ (Vitkevich & Vlasov 1970, Ekers & Little 1971, Scott, Coles & Bourgois 1983).

(e) The Source-Size Effect

As discussed in Section 2.12, the angular size of the source under observation has an appreciable effect on the shape of the IPS power spectrum. The power spectrum of an extended source is that for a point source filtered by the square of the source visibility. For a symmetrical Gaussian brightness distribution $B(\theta) = exp(-\theta^2/2\theta_\circ^2)$ the square of the visibility is $|V(q,z,\theta_\circ)|^2 = exp(-q^2z^2\theta_\circ^2)$, where $\theta_\circ$ is the radius of the source at the $e^{-\frac{1}{2}}$ level. The full width at half maximum is $\Theta_S = 2.35\theta_\circ$. Thus, the effect of the source size is to insert a filter function, attenuating frequencies above $q_s = 1/z\theta_\circ$.

Fig. 3.11 shows the effect of source size on the power spectrum for a solar-wind velocity of 400 kms^{-1}, a power-law index of $\alpha = 3.3$, an axial ratio of AR = 1.0 and a solar elongation of $\varepsilon = 20°$. We see that the power-law form of the high-frequency spectrum is attenuated by the source visibility function. If the source is small enough ($\Theta_S < 150$ mas), only the high-frequency power-law tail is affected and the source visibility has little effect on the Fresnel knee of the spectrum. However, if the source is large ($\Theta_S > 150$ mas), even the knee is affected. For estimating the parameters of the solar wind, we fit models to the

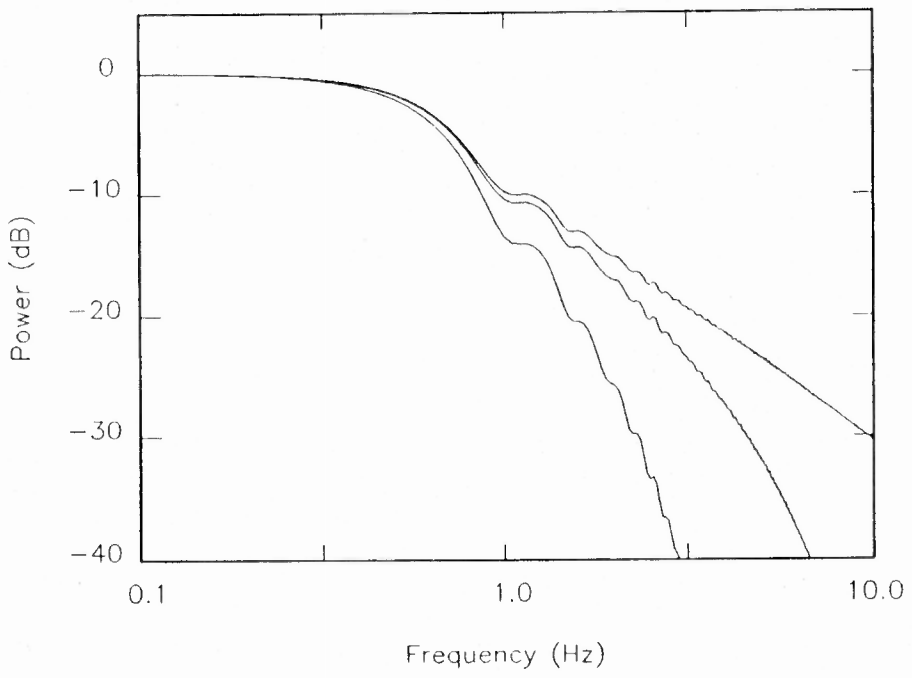

Fig. 3.11 Model spectra with velocity 400 kms^{-1} and $\alpha = 3.3$ showing the effect of source size. The source size $\Theta_S = 0\,mas$ for the top spectrum, $\Theta_s = 50\,mas$ for the middle spectrum and $\Theta_S = 150\,mas$ for the bottom spectrum. The spectra are computed for the solar elongation $\varepsilon = 20°$.

spectra of observed data, using the Fresnel knee as a fitting aid. As the power-law index and the source size affect the knee in a similar manner, fitting for a large source of unknown size can lead to systematic errors if the spectrum has a low signal-to-noise ratio ($\approx$ 15 dB). However, if the signal-to-noise ratio of the spectrum is good ($\geq$ 25 dB) and the high-frequency tail has sufficient power, fitting the high-frequency portion can discriminate between the two effects. A large source size usually gives a low scintillating flux density, producing little scintillating power and resulting in a power spectrum of low signal-to-noise ratio. Therefore, if the source size is large ($\Theta_S > 150$ mas), one should have *a priori* knowledge of the source size to avoid systematic errors in the estimated parameters.

If the position angle of an elongated source changes with respect to the Sun, we should use the source size projected along the direction defined by the velocity of the solar wind if we are to avoid biases in the estimated velocities (see Section 3.4.4 c in respect of axial ratio). Thus, the source-size parameter plays a major role in the fitting process and must be considered carefully. Most of the sources we have observed have been well studied at low frequencies using the VLBI techniques. In Appendix A, we list the adopted source sizes for spectral fitting.

(f) The Inner-Scale

Another important parameter which affects the shape of the spectrum is the 'smallest-scale' or 'inner-scale' present in the IP medium. The term 'inner-scale' is used in studies of turbulent fluid. If S_i is the smallest scale size of the irregularities of the medium, with an absence of irregularities much smaller than this, then the spectrum of electron-density fluctuations $\Phi_{\Delta N_e}(q)$ falls rapidly above $q_i \approx \frac{1}{S_i}$. This type of characteristic 'cut-off' observed at high wavenumber indicates the presence of an 'inner-scale' (refer eqn. 2.81).

The estimation of the electron-density spectrum based on IPS observations (Coles 1978, Scott, Coles & Bourgois 1983), spacecraft experiments (Yakovlev *et al.* 1980) and recent radar experiments (Coles & Harmon 1989) indicate the existence of a dissipative process that affects scale sizes smaller than an 'inner-scale', S_i, which attenuates the electron-density fluctuation spectrum. Hence, the intensity spectrum falls sharply at high frequencies in a fashion similar to the source-size cut-off. The break in the spatial wave number q_i, caused by the 'inner-scale' is defined to be $q_i = \frac{3}{S_i}$ (Coles & Harmon 1989).

At a given temporal frequency in the power spectrum, the source-size filter effect decreases as our line-of-sight moves farther from the Sun and the effective distance to the screen decreases. (This is as the source visibility, $|V(q, z, \theta_o|$ does not produce a sharp cut-off for smaller z-distances to the screen.) However, for a given 'inner-scale' size, the break frequency in the power spectrum remains the same for all screen distances. Hence, differentiating between the 'inner-scale' and source-size effects is possible for large elongations, corresponding to smaller z. However, it is much simpler to estimate the 'inner-scale' size if the source size is known. Our model used for the computation of the temporal spectrum includes the effect of the 'inner-scale'. Many observations with the ORT have high scintillating power and this results in a smooth spectrum extending to high temporal frequencies. This enables us to fit the 'inner-scale' size for sources of small, but known, angular extent.

3.5 Summary

In this chapter, we have described the computational details for obtaining the power spectrum of an observation and its scintillation index. We have also given

the details of the logarithmic averaging adopted to suit our power-spectrum fitting procedure and described the computation of the model spectrum for various solar-wind parameters, assuming a spherically-symmetric solar wind. The sensitivity of the model spectrum to the various solar-wind parameters has been discussed. The model fitting described in the next chapter is based on observations in the weak-scattering regime.

3.6 References

Ananthakrishnan, S., 1976. Ph.D. Thesis, University of Bombay.

Armstrong, J.W. & Coles, W.A., 1978. Astrophys. J., **220**, 346.

Blackman, R.B. & Tukey, T.W., 'The Measurement of Power Spectra from the Point of Communication Engineering', 1959, Dover Publications Inc., New York.

Blessing, R.G. & Dennison, P.A., 1972. Proc. Astr. Soc. Australia,**2**, 84.

Coles, W.A., 1978. Space Sci. Rev., **21**, 411.

Coles, W.A. & Harmon, J.K., 1989. Astrophys. J., **337**, 1023.

Coles, W.A. & Kaufman, J.J., 1978. Radio Sci., **13**, 591.

Ekers, R.D. & Little, L.T., 1971. Astr. Astrophys., **10**, 310.

Joshi, M.N., Swarup, G., Bagri, D.S. & Kher, R.K., 1988, Bull. Astr. Soc. India, **16**, 111.

Kojima, M., 1979. Publ. Astron. Soc. Japan, **31**, 231.

Kraus, J.D., 'Radio Astronomy', 1966, McGraw-Hill Book Company, New York.

Rao, A.P., 1975. Ph.D. Thesis, University of Bombay.

Rao, A.P., Bhandari, S.M. & Ananthakrishnan, S., 1974. Aust. J. Phys., **27**, 105.

Readhead, A.C.S, 1971. Mon. Not. R. astr. Soc., **155**, 185.

Scott, S.L., Coles, W.A. & Bourgois, G., 1983. Astr. Astrophys., **123**, 207.

Swarup, G., Sarma, N.V.G., Joshi, M.N., Kapahi, V.K., Bagri, D.S., Damle, S.H., Ananthakrishnan, S., Balasubramanian, V., Bhave, S.S. & Sinha, R.P., 1971. Nature Phys. Sci., **230**, 185.

Venugopal, V.R., Ananthakrishnan, S., Swarup, G., Pynzar, A.V. & Udaltsov, V.A., 1985. Mon. Not. R. astr. Soc., **215**, 685.

Vitkevich V.V. & Vlasov, V.I., 1970. Sov. Astronomy, **13**, 669.

Woo, R. & Armstrong, J.W., 1979. J. Geophys. Res., **84**, 7288.

Yakovlev, O.I., Efimov, A.I., Razmanov, V.M. & Shtrykov, V.K., 1980. Sov. Astronomy, **24**, 454.